Electronic Supplementary Information (ESI) for ChemComm.

Poly(ionic liquid)-based polymer composites as high-performance solid-state electrolytes: benefit from nanophase separation and alternating polymer architecture

Meng Zhang, Quan Zuo, Lei Wang, Songrui Yu*, Yiyong Mai*, and Yongfeng Zhou *

School of Chemistry and Chemical Engineering, Frontiers Science Center for Transformative Molecules, State Key Laboratory of Metal Matrix Composites, Shanghai Key Laboratory of Electrical Insulation and Thermal Ageing, Shanghai Jiao Tong University, 800 Dongchuan Road, Shanghai 200240, China.

E-mail: tracyyu@sjtu.edu.cn; mai@sjtu.edu.cn; yfzhou@sjtu.edu.cn

Content

1. Methods

1.1 Chemicals.

Poly(vinylidene fluoride-co-hexafluoropropylene) (PVDF-HFP) (Elf Atochem, Knyar® 2801) was dried in vacuum at 110 ℃ for 24 h before use. Dichloromethane (DCM) (Greagent, ≥99.5%) was dried over calcium hydride and distilled before use.
Poly(ethylene glycol) diglycidyl ether (PEGDE) (Sigma-Aldrich, M_n ~ 500), Poly(ethylene glycol) diglycidyl ether (PEGDE) (Sigma-Aldrich, M_n ~ 2000), 1,4-butanedithiol (BDT) (TCI, 95%), triethylamine ($N(Et)_3$) (Acros, 99.0%), methanol (Greagent, 99.5%+), ethyl ether (Sinopharm, AR), 1-methylimidazoles (NMI) (Adamas, 99.0%), *p*-toluenesulfonyl chloride (TsCl) (General-Reagent, 99.0%), sodium hydrogen carbonate ($NaHCO_3$) (Greagent, ≥99.5%), sodium chloride (NaCl) (Greagent, ≥99.5%), sodium dihydrogenorthophosphate (NaH_2PO_4) (Greagent, ≥99.5%), sodium sulfate (Na_2SO_4) (Greagent, ≥99.5%), lithium bis(trifluoromethanesulfonyl)imide (LiTFSI) (J&K, 99%), ethanol (Greagent, ≥99.7%), dimethylformamide (J&K, ⩾ 99.8%) were used as received without purification.

1.2 Instruments and measurements

Nuclear Magnetic Resonance (NMR):
^{1}H NMR spectra were recorded on Bruker Avance III 500 (500 MHz, Bruker) with chloroform-d ($CDCl_3$) as solvent at 25 ℃. ^{13}C NMR spectra were recorded on Bruker Avance NEO 700 (700 MHz) spectrometer with dimethylsulfoxide-d_6 (DMSO-d_6) as solvents at 25 ℃. Tetramethylsilane (TMS) was used as an internal standard.

Differential Scanning Calorimeter (DSC):
DSC analyses were carried out on a TA Q2000 apparatus under nitrogen flow. Three cycles were performed for each sample to eliminate thermal history. Cycle I: increasing temperature from 40 ℃ to 200 ℃ with a heating rate of 20 ℃/min, and isothermal 1 min; Cycle II: decreasing temperature from 200 ℃ to -80 ℃ with a cooling rate of 10 ℃/min, and isothermal 5 min; Cycle III: increasing temperature from -80 ℃ to 200 ℃ with a heating rate of 10 ℃/min. The 3rd cycle of data was used for comparation of glass transition and melting temperature

Thermogravimetric Analysis (TGA):
TGA were performed on a Discovery TGA550 apparatus from T.A. Instruments under nitrogen flow. The heating process started from 50 ℃ to 800 ℃ with a heating rate of 10 ℃/min.

Gel Permeation Chromatography (GPC):
The molar mass of a polymer samples were measured by GPC on a HLC-8320 system at 40 ℃ with THF as mobile phase at a flow rate of 1.0 mL/min, or on a

HLC-8320XX with DMF as mobile phase at a flow rate of 1.0 mL/min (for PPaB-MT-43).

Fourier-transform Infrared Spectroscopy (FTIR):
Viscous polymer samples were firstly dissolved in DCM and then casted onto pure KBr pellets. After fully dried, the pellets were ready for FTIR. FTIR spectra were recorded on a Perkin Elmer Spectrum 100 spectrophotometer in the range of 4000 - 450 cm^{-1}.

Dynamic Thermomechanical Analysis (DMA):
The mechanical strength of samples were carried out on a Discovery DMA850 apparatus from T.A. Instruments at 25 ℃ using rate control mode. The samples were cut into strips 5 mm wide and 20 mm long.

Transmission Electron Microscopy (TEM):
TEM measurements were performed on a TALOS F200X operationg with an accelerating voltage of 200 kV.
The film samples were cut into strips 1 mm wide and embedded in epoxy resin (Buehler, Lake Bluff, IL). Embedded samples were cut into thin slices of approximately 100 nm, using the UC6-FC6 cryo-ultramicrotome from Leica Microsystems, Germany and collected on carbon-coated copper grids for TEM characterization.

Atomic Force Microscopy (AFM):
AFM measurements were carried out on a BioScope Resolve spectrometer (Bruker Corporation, USA) by using tapping mode at room temperature. The samples for AFM observations were prepared by casting several drops of PPaB-MT/PVDF-HFP/LiTFSI solution on glass and dried in vacuum at 70 ℃ for 24 h.

Linear sweep voltammetry (LSV):
The electrochemical stability window of the polymer electrolytes was evaluated by linear sweep voltammetry (LSV) using a ss|SPE|Li cell on the electrochemical workstation CHI 600d.
LSV was performed from 2.0 V to 5.5 V with a scanning rate of 0.5 mV/s.

Ionic conductivity:
The measurement of ionic conductivity (σ, in $S \cdot cm^{-1}$) of the polymer electrolyte was carried out on an Autolab PGSTAT302N electrochemical workstation (Metrohm, Switzerland) using electrochemical impedance spectroscopy (EIS) technique. The membranes of blended polymer electrolytes were sandwiched between a pair of stainless steel (ss) blocking electrodes and fabricated in an argon-filled glovebox (O_2 < 0.1ppm, H_2O < 0.1ppm) using CR2016 coin-type cells by a lamination process. Before measuring, the cells were heated at 60 ℃ for 2h for allowing good contact

between electrolytes and electrodes. The ac impedance spectra were recorded in the frequency range from 0.1 to 10^6 Hz over the temperature range from 25 to 85 ℃. The cell was thermally equilibrated at each temperature for at least 2h prior to measurement. The temperature of the cell was accurately controlled in a drying oven.

Interfacial Compatibility:
The interfacial compatibility of the polymer electrolytes were evaluated by A.C. Impedance experiments using a Li metal | SPE | Li metal cell for varying storage times using at room temperature. The measurements were taken on the electrochemical workstation CHI 760e in the frequency range from 0.1 to 10^5 Hz with an oscillation voltage of 5 mV.

Li stripping and deposition experiments:
Li stripping and deposition experiments were taken on Land CT2001A (Land, China) using a Li metal | SPE | Li metal cell.

1.3 Preparation of polyelectrolyte films

In a typical preparation process, P(PEGDGE-*a*-BDT)-MIM/TFSI, PVDF-HFP and LiTFSI were dissolved in DMF and mixed ultrasonically for 24 h to obtain a homogenous solution. Then the viscous solution was cast into a polytetrafluoroethylene mold and dried in vacuum at 70 ℃ for 48 h. The obtained films were cut into small round pieces with a diameter of 1.9 cm for lithium battery use. The average thickness of the resulted films was about 70 μm (measured by screw micrometer).

1.4 Synthesis and characterization of alternate structured poly(ionic liquid) P(PEGDGE-*a*-BDT)-MIM/TFSI

The PIL, P(PEGDGE-a-BDT)-MIM/TFSI (denoted as PPaB-MT), was synthesized following the procedures as below: (i) Alternating copolymer P(PEGDGE-a-BDT) (abbreviated as PPaB) was synthesised by the thiol-epoxy click reaction of poly(ethylene glycol) diglycidyl ether (PEGDGE) and 1,4-butanedithiol (BDT). (ii) Partial hydroxyl groups on PPaB were converted to tosylates, yielding PPaB-OTs. (iii) Cationic 1-methylimidazole (MIM) groups were grafted onto the polymer according to a reported procedure, [1] producing the PPaB-MO copolymer. In this step, OTs (Ts = p-toluenesulfonyl (tosyl)) groups detached from the polymer backbone and were trapped in the PPaB-MO as the counter-ions of the MIM cations. [2] (iv) The final product, PPaB-MT was obtained by exchanging OTs anions with bis(trifluoromethanesulfonyl)imide (TFSI) anions.

1.4.1 Synthesis of alternating copolymer P(PEGDGE-*a*-BDT)

P(PEGDGE-*a*-BDT) was synthesized according to previous literatures reported by our group.[3] The detail synthesis process was as follow: poly(ethylene glycol) diglycidyl ether (25.0 g, 50 mmol) was firstly dissolved in 150 mL methanol and purged with highly pure N_2 gas for 1 h to eliminate oxygen. Then 1,4-butanedithiol (6.1 g, 50 mmol) and triethylamine (12.0 mL) were added into the solution successively. After reacting for 48 h at room temperature, the solution was concentrated and dropped slowly into a large amount of cold ethyl ether. The purification process was repeated three times and the light yellow precipitates were collected. The final products P(PEGDGE-*a*-BDT) were dried under vacuum at 60 °C and the yield was 84%.

1.4.2 Synthesis of tosylated alternating copolymer P(PEGDGE-*a*-BDT)-OTs

Partial hydroxyl groups on PPaB were converted to tosylates, yielding PPaB-OTs.[4] P(PEGDGE-*a*-BDT) (9 .72g, ca. 30 mmol OH group) and 150 mL DCM were added into a 300 mL single-neck round-bottom flask and stirred to dissolve completely. Subsequently, dried triethylamine (8.4 ml, 60 mmol) and NMI (1.2 ml, 15 mmol) was added to the above solution. Then, a solution of TsCl (8.53 g, 45 mmol, 1.5 equiv) in DCM (50 mL) was added into the previous mixture dropwise from a pressure equalizing dropping funnel and kept stirring at room temperature for 24 h. The crude solution was extracted with 20 % sat. $NaHCO_3$ (50 mL) for three times, and the DCM phase was collected and dried with Na_2SO_4. After evaporation of DCM, the crude product was dropped slowly into cold ethyl ether (2 L, -30 ℃). The purification process was repeated three times and the light brown viscous intermediate product P(PEGDGE-*a*-BDT)-OTs was collected and dried at 60 ℃ in vacuum for 48 h.

1.4.3 Synthesis of imidazole-based alternating copolymer P(PEGDGE-*a*-BDT)-MIM/OTs

Refer to the synthetic process published by Mülhaupt et al.[1], P(PEGDGE-*a*-BDT)-OTs (8.32 g, ca. 10 mmol OTs) prepared as above and 1-methylimidazole (16 mL, 200 mmol) were mixed in a 50 mL single-neck round-bottom flask and stirred continuously at 120 °C for five days. Then the crude product was concentrated and dialyzed against (MWCO: 3500 Da) methanol for seven days. After removal of the solvents and being dried in vacuum at 60 ℃ for 48 h, the product P(PEGDGE-*a*-BDT)-MIM/OTs was collected with a final yield of 75%.

1.4.4 Synthesis of alternate structured poly(ionic liquid) P(PEGDGE-*a*-BDT)-MIM/TFSI

P(PEGDGE-*a*-BDT)-MIM/TFSI was obtained by an ion exchange reaction.[1,2] P(PEGDGE-*a*-BDT)-MIM/OTs (5 g, ca. 5 mmol) were dissolved in 100 mL deionized

water, followed by the addition of excess LiTFSI solution (1 M, 50 mL). After stirring 2 h, the turbid solution was dialyzed against (MWCO: 3,500 Da) ethanol and deionized water (1:1, v/v) for seven days and dried in vacuum at 60 ^{o}C for three days, the final product P(PEGDGE-*a*-BDT)-MIM/TFSI was obtained as a viscous dark brown liquid.

The synthesis of reference polymer P(PEGDGE-*a*-BDT)-MIM/TFSI with longer PEG segments was realized by replacing the shorter PEGDGE (n=9) by a longer PEGDGE (n=43). Except for this only difference, the synthesis followed the same protocol as the synthesis of PPaB-MT (n=9) as describe above. The final product was abbreviated as PPaB-MT-43.

2. Additional data

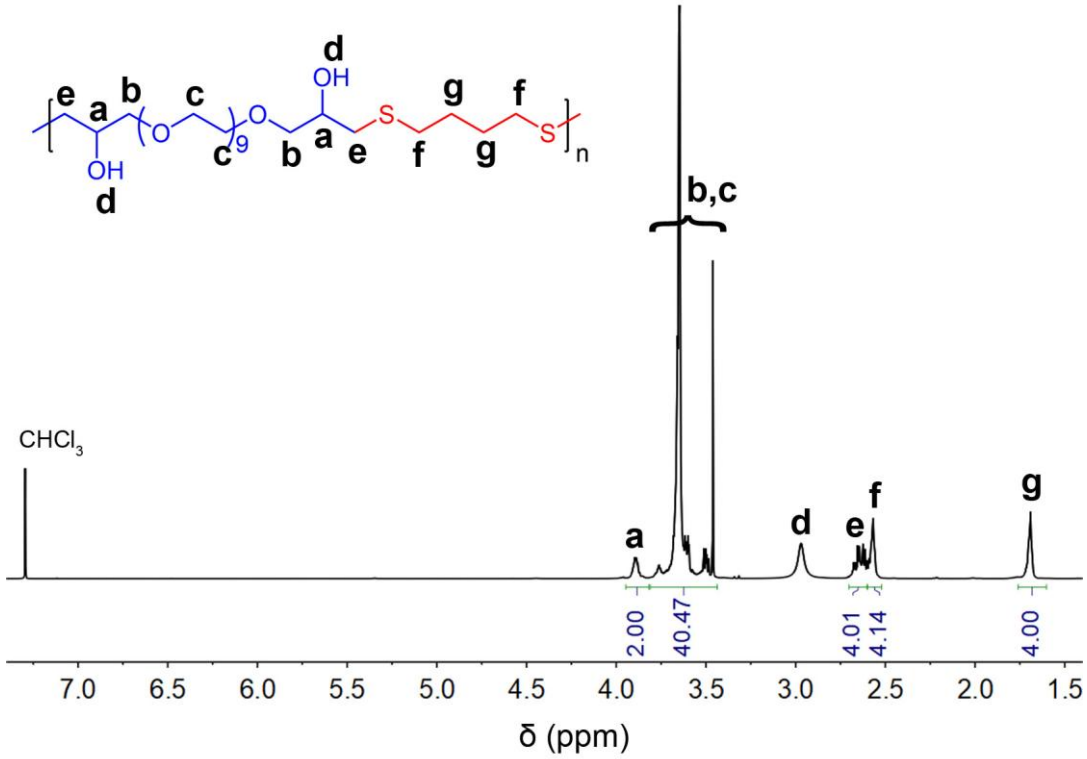

Fig. S1 ^{1}H NMR spectrum of the alternating copolymer PPaB ($CDCl_3$, 298K). All peaks are well assigned and the corresponding protons are marked in the molecular structure.

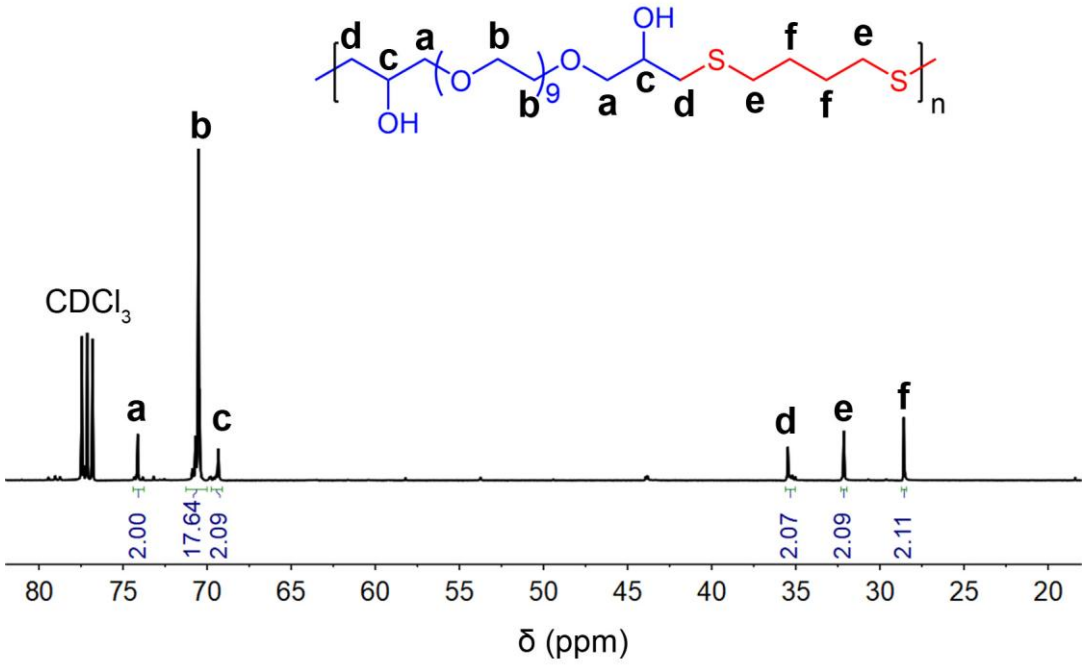

Fig. S2 Quantitative ^{13}C NMR spectrum of the alternating copolymer PPaB ($CDCl_3$, 298K). All peaks are well assigned and the corresponding carbon atoms are marked in the molecular structure.

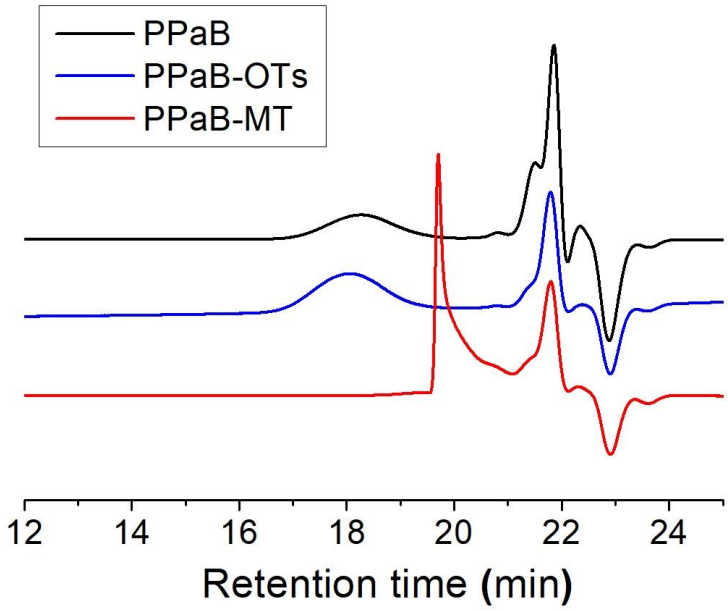

Fig. S3 GPC traces (THF) of intermediate and final products. Black line: alternating copolymer PPaB; Blue line: intermediate product PPaB-OTs; Red line: final PIL PPaB-MT. The molar mass of PPaB was measured to be 10,100 g mol^{-1}, and dispersity (Đ) of 1.6; molar mass of PPaB-OTs was 11,000 g mol^{-1}, and Đ = 1.5. The GPC chromatogram of PIL PPaB-MT, which is supposed to have a shorter retention time because of the larger molar mass of MIM/TFSI than OTs, showed a sharp and unreasonable peak with longer retention time. It has been demonstrated that, the charged groups of PILs make it complicated and unreliable to characterize the molar mass of PILs by using common GPC methods.[5]

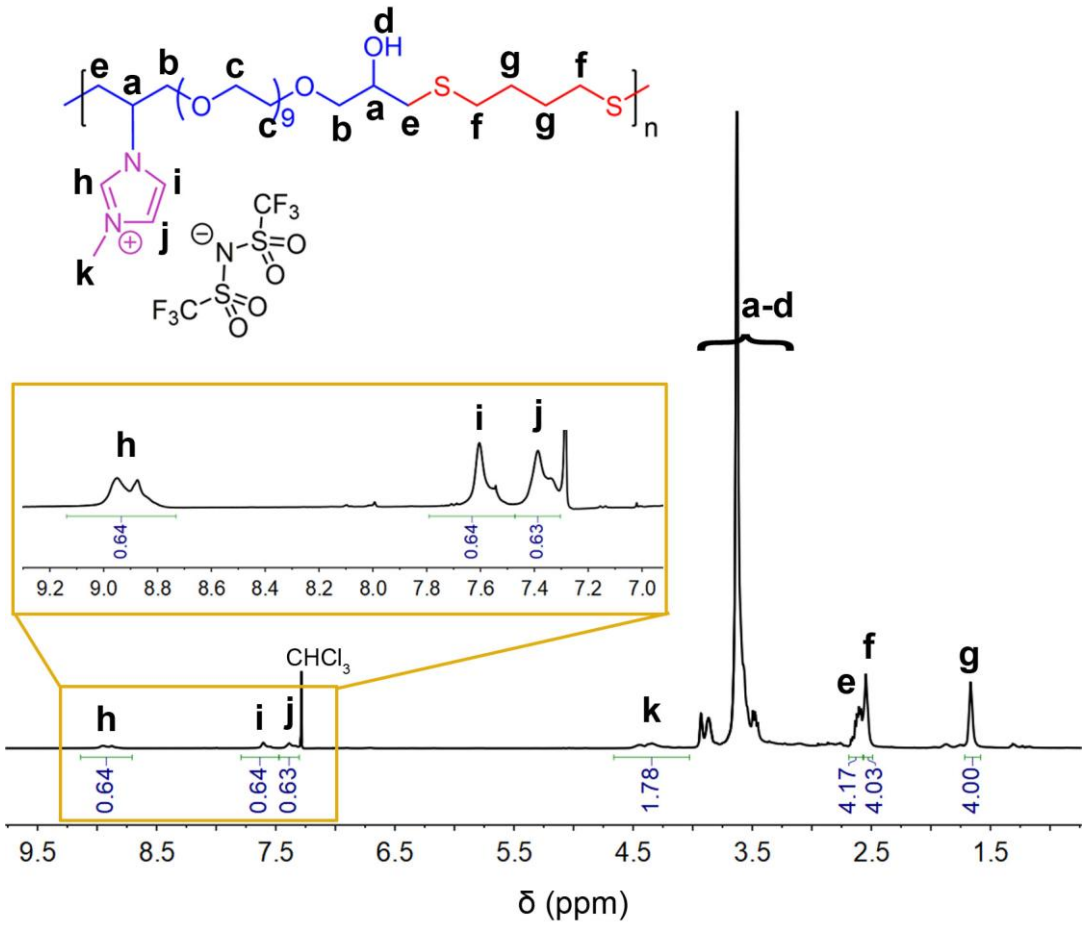

Fig. S4 ^{1}H NMR spectrum of PPaB-MT ($CDCl_3$, 298K). All peaks are well assigned and the corresponding protons are marked in the molecular structure.

The conversion ratio of hydroxyl groups to MIM/TFSI groups can be calculated according to equation (1):

$$\phi = \frac{\mathrm{A(h)\ [or\ A(i)\ or\ A(j)]}}{\mathrm{A(t,\ -OH)}} \times 100\% \qquad (1)$$

A(h), A(i) and A(j) represent the integration area of peak h, i and j, respectively. A(t, -OH) is the theoretical peak area of hydroxyl groups in the first step product PPaB, which should be 2 here because the peak g is normalized to 4 in this spectrum. Therefore, ~ 32% of hydroxyl groups in PPaB were converted to MIM/TFSI groups in the final product of PPaB-MT.

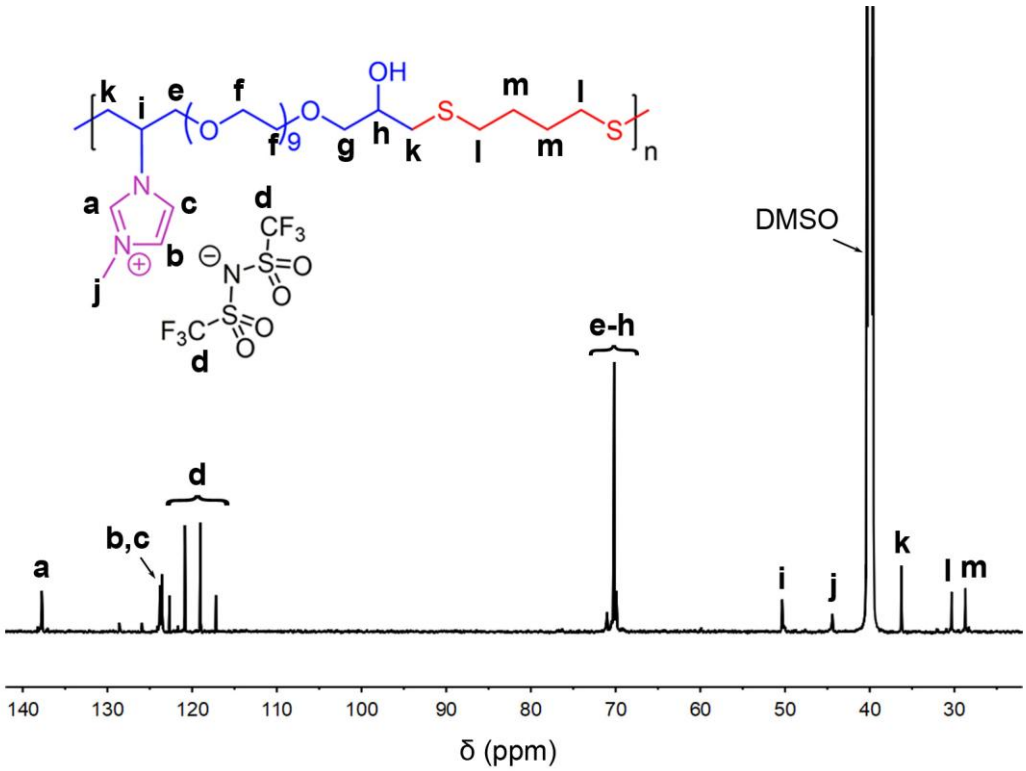

Fig. S5 ^{13}C NMR spectrum of PPaB-MT (DMSO-d6, 298K). All peaks are well assigned and the corresponding carbon atoms are marked in the molecular structure.

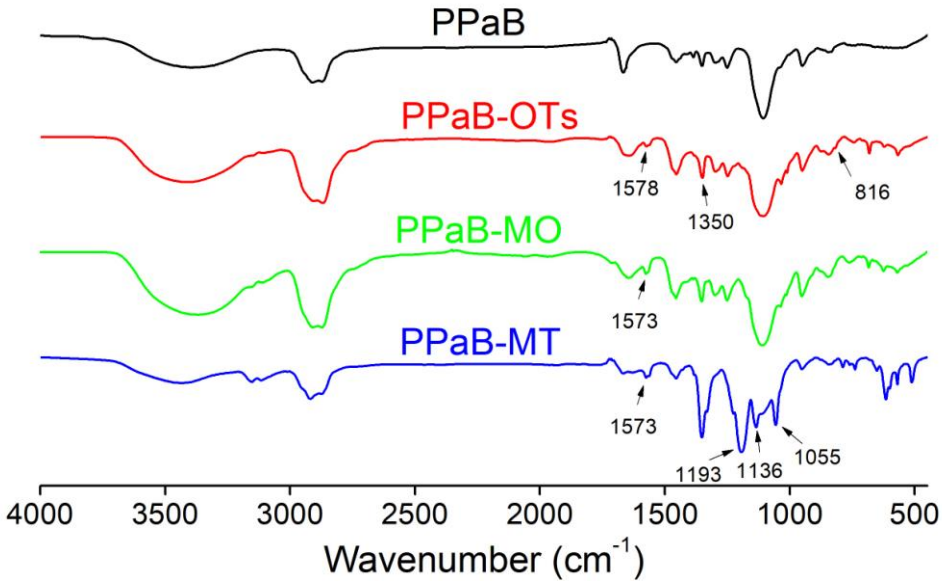

Fig. S6 FTIR spectra of PIL and the intermediate products. Black line: PPaB; Red line: PPaB-OTs; Green line: PPaB-MO; Blue line: PPaB-MT. Compared with original polymer PPaB, the stronger absorbance at 1350 cm^{-1} and new absorbance at 1578 cm^{-1} in PPaB-OTs could attribute to -SO_2- and aromatic C=C bonds in OTs groups, respectively.[2] The new peak at 816 cm^{-1}, which is related to the C-O-S bonds,[6] indicates the covalent bonding of OTs onto the polymer. The conversion of OTs to MIM/OTs groups in PPaB-MO can be proved by the stronger absorbance at 1573 cm^{-1}, which is attributed to the C=N bonds in MIM groups. Moreover, the absence of peak at 816 cm^{-1} indicates the OTs groups has detached from the polymer, and are supposed to be trapped in the polymer as counter-ions to MIM groups. Finally, besides the absorbance of MIM cations at 1573 cm^{-1}, the new absorbance at 1055 cm^{-1}, 1136 cm^{-1} and 1193 cm^{-1}, which can be assigned to symmetric stretching of -SO_2-N-SO_2-, symmetric stretching of -SO_2 and antisymmetric stretching of CF_3 in TFSI anions,[7,8] proved the successful preparation of PPaB-MT.

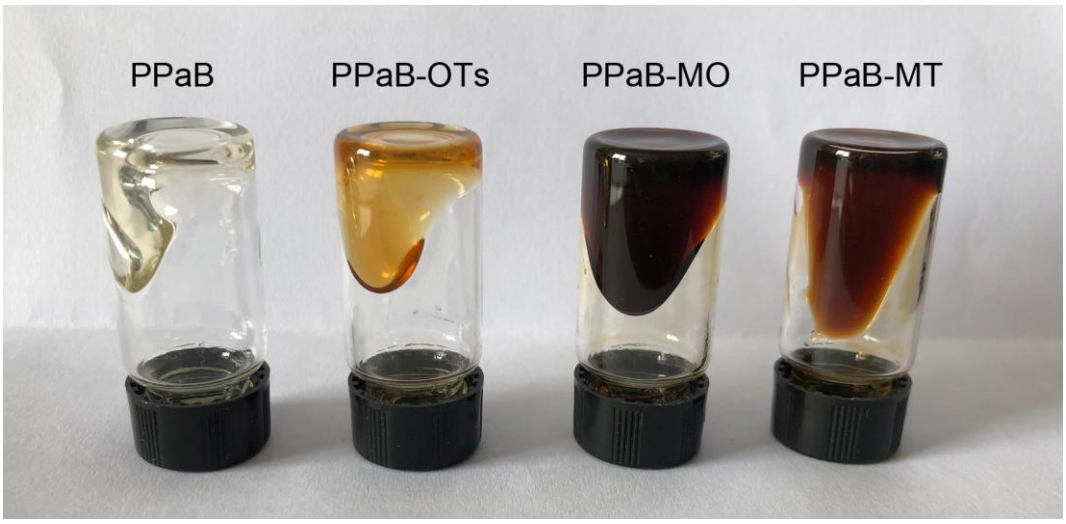

Fig. S7 Photographs of PPaB-MT and its intermediate products. Vials from left to right contain PPaB, PPaB-OTs, PPaB-MO and PPaB-MT, respectively. Photos were taken after the vials stayed reversely for 1 min at 25 ^{o}C.

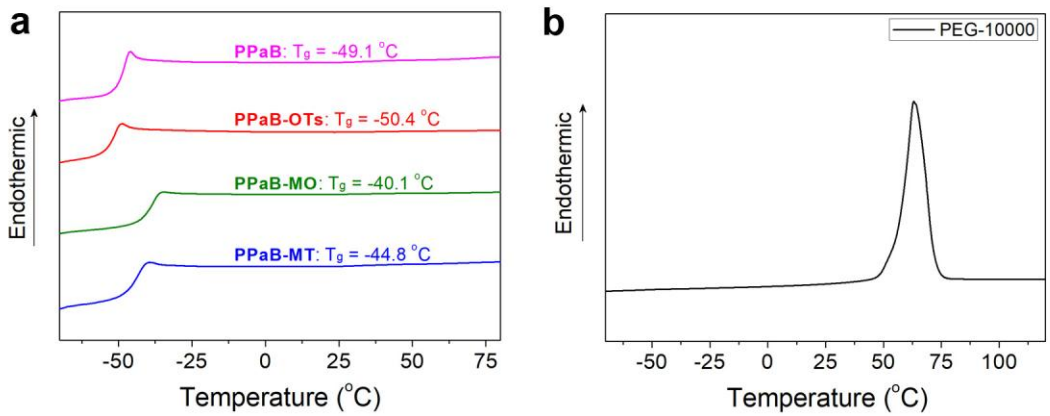

Fig. S8 DSC traces of (a) PPaB-MT and its intermediate products, and (b) a reference polymer PEG-10000. Lines in (a): Pink line: PPaB; Red line: PPaB-OTs; Olive line: PPaB-MO; Blue line: PPaB-MT. The reference PEG has a comparable molar mass (M_n = 10,000 g mol^{-1}) with PPaB-MT. PEG-10000 shows no T_g but a very sharp melting peak at ~ 62 °C, while PPaB-MT and its intermediate products possess very low T_gs but no melting transitions.

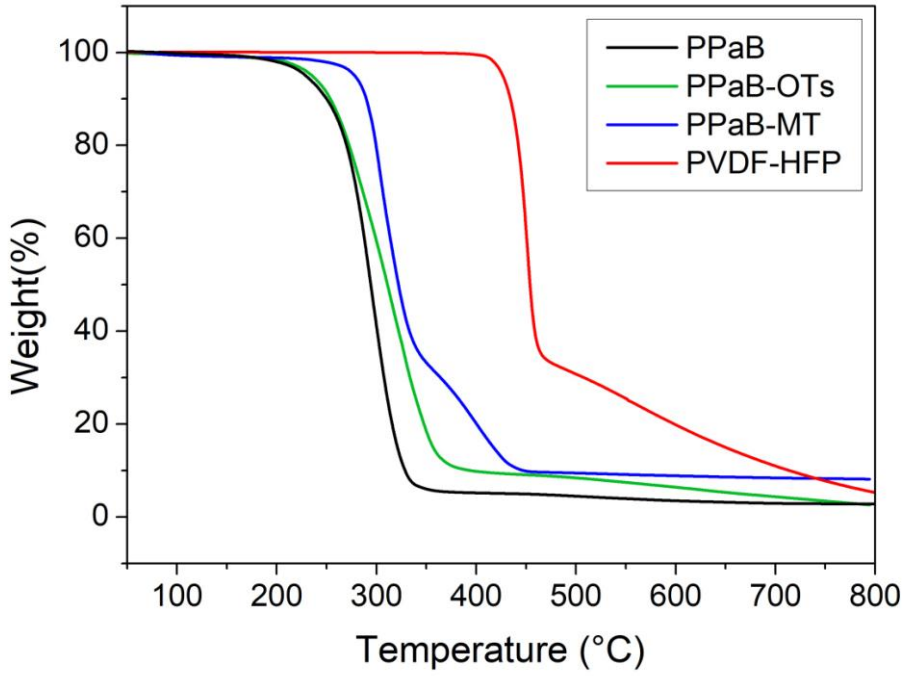

Fig. S9 TGA analysis of PPaB, PPaB-OTs, PPaB-MT and PVDF-HFP. PPaB-MT shows a decomposition temperature over 270 ^{o}C and PVDF-HFP over 420 ^{o}C. Therefore, SPEs based on PPaB-MT/PVDF-HFP blends may have a high operation temperature up to 270 ^{o}C. Interestingly, the decomposition temperatures of products of first two steps, PPaB and PPaB-OTs, are ca. 40 ^{o}C lower than that of PPaB-MT. It indicates that grafting ionic liquid moieties (MIM/TFSI) onto the polymer chain could improve the thermostability of the resulted polymer.

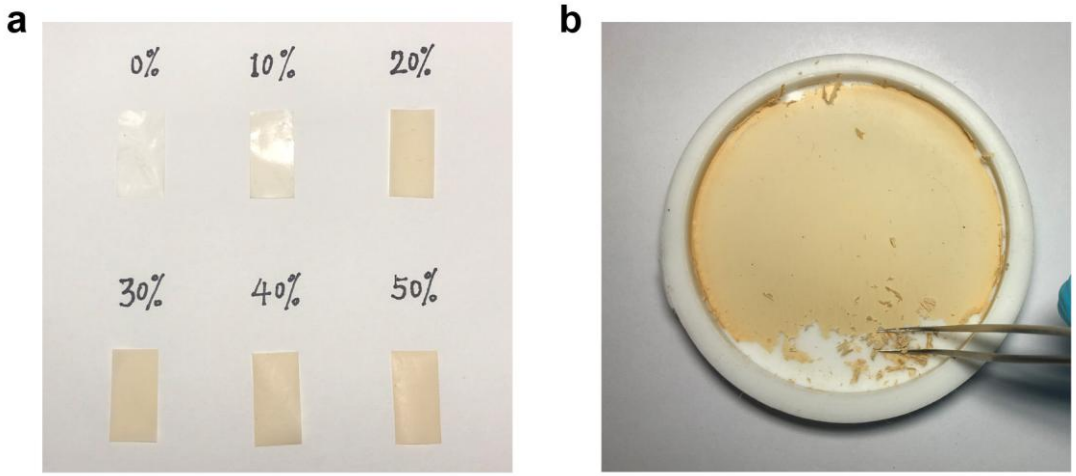

Fig. S10 Photos of PPaB-MT/PVDF-HFP/LiTFSI films with different compositions. The PPaB-MT contents in SPE films in (**a**) are 0 wt%, 10 wt%, 20 wt%, 30 wt%, 40 wt% and 50 wt%. These films are free-standing and cut into 2 cm × 1 cm pieces for photography. (**b**) The film with a 60 wt% content of PPaB-MT is soft, fragile and cannot be peeled off intactly from the PTFE mould. The weight percent of PPaB-MT refers to the weight ratio of that of PPaB-MT in the total weight of PPaB-MT and PVDF-HFP, without involving in LiTFSI salts. All films contain 20 wt% LiTFSI salts.

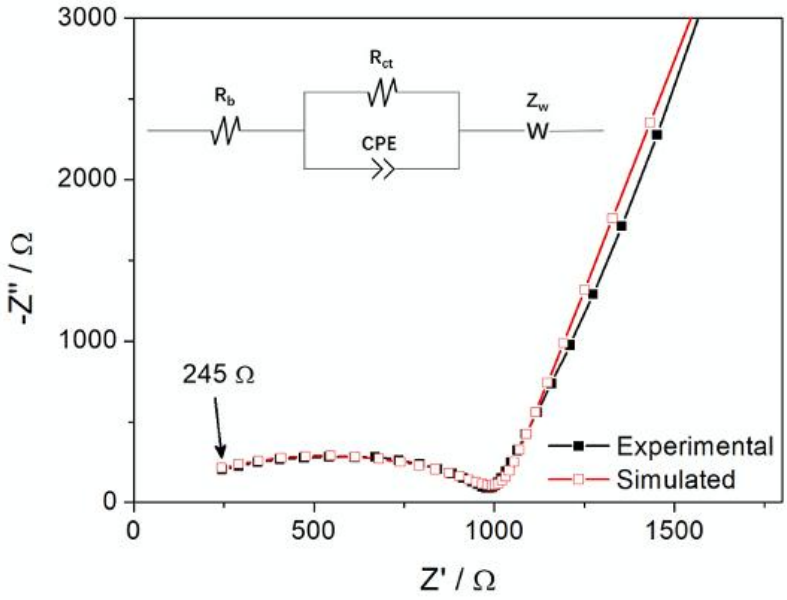

Fig. S11 Electrochemical Impedance spectra for the PPaB-MT/PVDF-HFP/LiTFSI (PPaB-MT content: 50 wt%) SPEs on the ss | SPEs | ss cell at 25 ℃. The calculation of ionic conductivity (σ) is identical with a previous work[9] and briefly described as blow: σ = l/(A·R), where l (cm) is the thickness of membranes, A (cm^2) is the area of stainless-steel blocking electrode, and R (Ω) is the resistance determined from the Nyquist plot (Fig. S11).

We fitted the experimental electrochemical impedance spectroscopy by using a simulated equivalent circuit (inset of Fig. S11). In this circuit, R_b represents bulk resistance (245 Ω according to the simulation), R_{ct} refers to charge transfer resistance (740 Ω), and Z_w is the Warburg impedance.

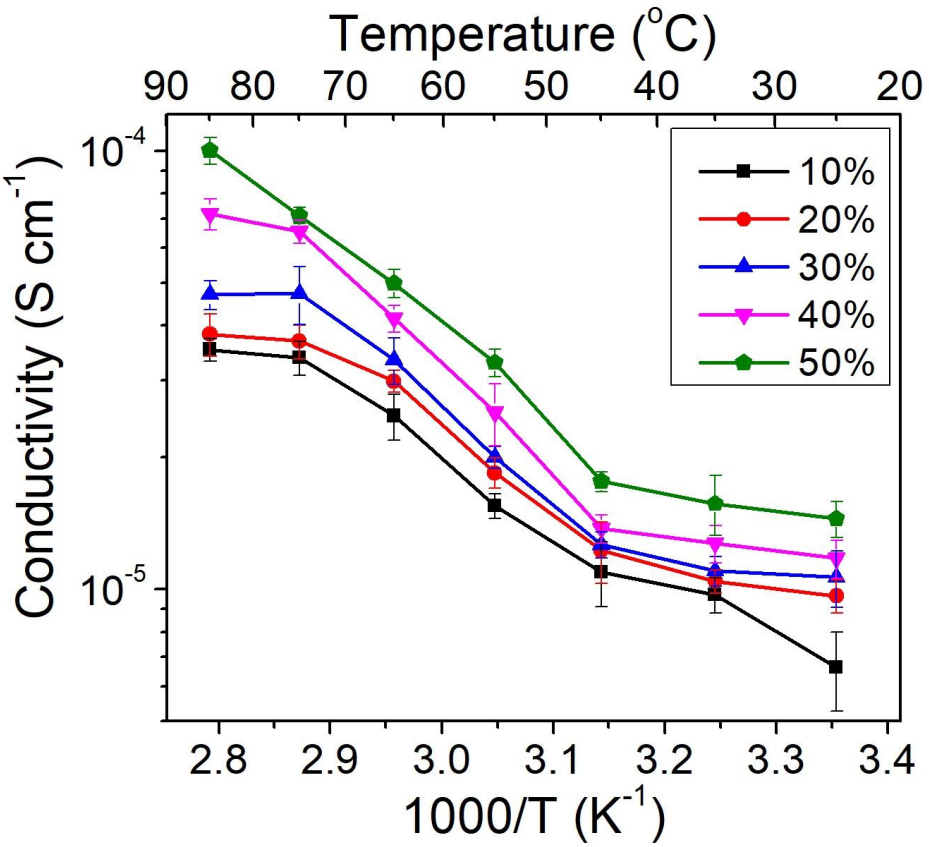

Fig. S12 Temperature dependence of the ionic conductivity of the PPaB-MT/PVDF-HFP/LiTFSI SPE films with different compositions. Each datum point was averaged over three measurements.

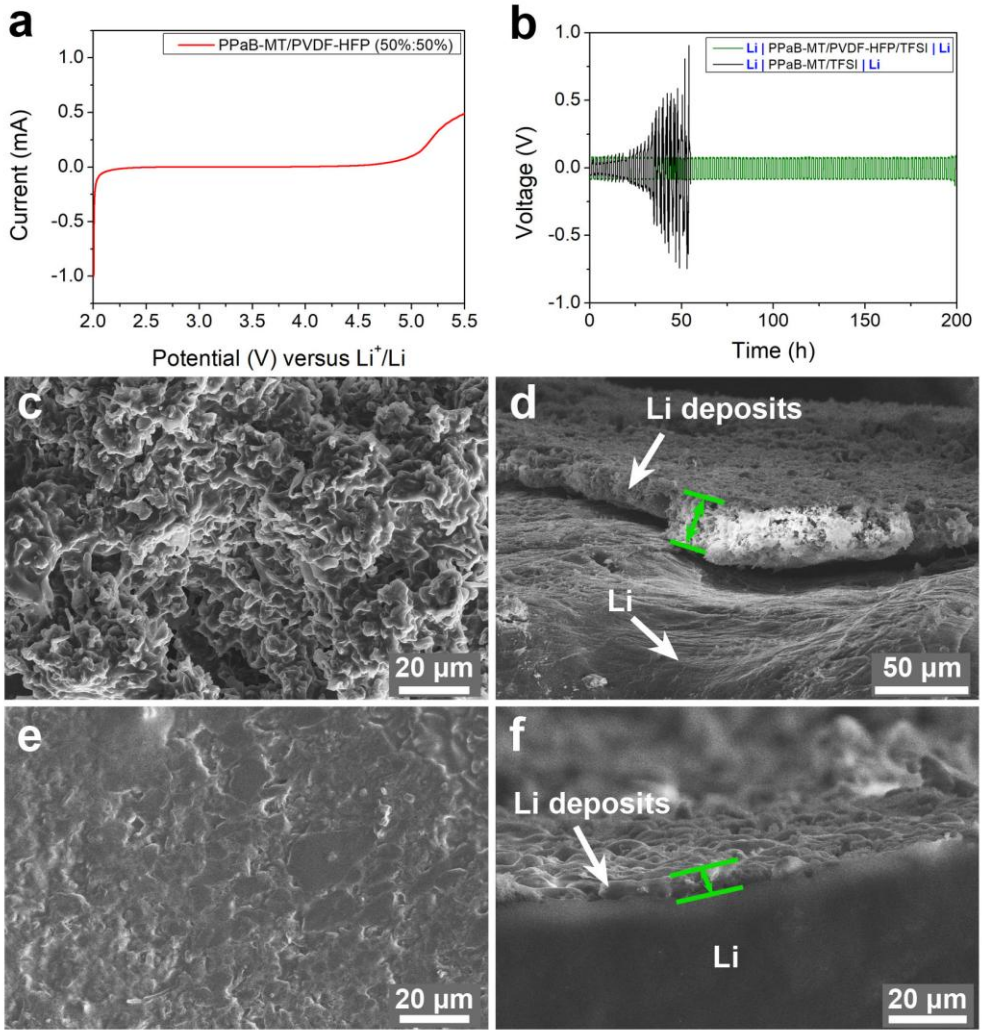

Fig. S13 Electrochemical stability and Li stripping/deposition studies. (a) Linear sweep voltammetry (LSV) for SPE with a composition of PPaB-MT/PVDF-HFP (50/50 w/w) at 25 ^{o}C. (b) Voltage profiles of the Li stripping and deposition process (current density: 0.1 mA cm^{-2}; capacity: 0.1 mAh cm^{-2}). (c,d) SEM images of Li deposition in Li | PPaB-MT | Li cells after cycling for 48 h. (e,f) SEM images of Li deposition in Li | PPaB-MT/PVDF-HFP | Li cells after cycling for 48 h. The weight ratio between the two polymers is 1:1.

The electrochemical stability window against lithium metal was studied by Linear Sweep Voltammetry (LSV) in the stainless steel | SPE | Li cells sweeping from 2.0 to 5.5 V at a constant rate of 0.5 mV s^{-1} at 25 ^{o}C. The voltage window of PPaB-MT/PVDF-HFP electrolytes with a PIL content of 50 wt% was stable up to ~ 4.7 V versus Li^{+}/Li (Fig. S13a), thus showing a relatively high stability of the SPE.

To investigate if the high mechanical strength of the SPEs could suppress the growth of Li dendrite, Li stripping and deposition experiments were carried out. Li | PE | Li symmetric cells were assembled by using PPaB-MT/PVDF-HFP as the polymer electrolyte or pure PPaB-MT as a control sample. It is notable that pure PPaB-MT is a viscous fluid rather than a solid, and therefore, it lacks mechanical strength (Fig. S7). It is found that the cell composed by pure PPaB-MT requires a smaller overpotential (50 mV) than the cell with PPaB-MT/PVDF-HFP SPEs (80 mV) for stripping and deposition during the initial cycles (Fig. S13b), which probably stems from a better affinity between the fluid PPaB-MT with electrodes and thus a lower resistance.[10,11] However, the overpotential of Li | PPaB-MT | Li cell started to increase exponentially after 10 charge-discharge cycles for 20 h and irregular voltage fluctuation was observed after 50 h. As a comparison, the cell with the PPaB-MT/PVDF-HFP SPE exhibits a highly stable voltage profile.

In order to disclose the underlying mechanism, SEM was carried out to study the Li deposition on the surface of electrodes (Fig. S13 c-f). A thick and porous layer of dead Li is detached from the electrodes in the control cell of Li | PPaB-MT | Li (Fig. S13d). Tremendous “needle-like” Li dendrites could be identified in the deposit layer (Fig. S13c). While in the cell assembled with the PPaB-MT/PVDF-HFP SPE, a thinner, smoother and more compact layer of Li deposits is visualized (Fig. S13 e,f), indicating that the growth of Li dendrites was successfully suppressed due to the high mechanical strength of the SPE.

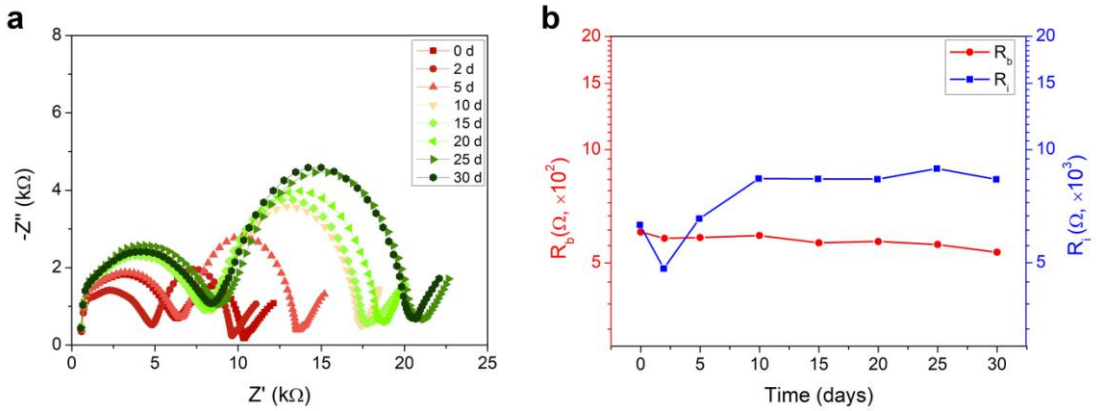

Fig. S14 Time dependence impedance spectroscopy of PPaB-MT/PVDF-HFP/LiTFSI (PPaB-MT content: 50 wt%) SPE film. (**a**) Nyquist plots of the impedance response on the Li | SPEs | Li cell at 25 ℃ at different time. (**b**) Time dependence of the bulk resistance (R_b) and the interfacial resistance (R_i) at 25 ℃.

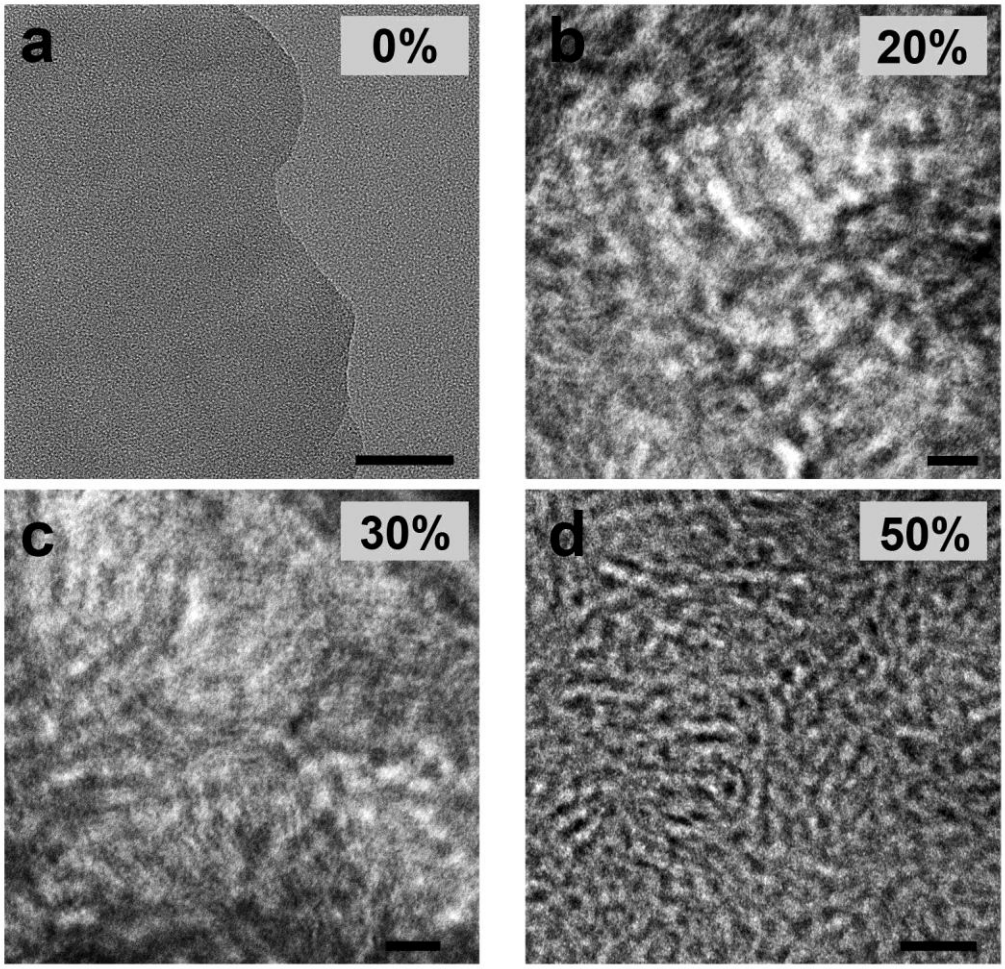

Fig. S15 TEM images of the SPE films with different PPaB-MT content. The film samples were embedded in epoxy resin and then cut into thin slices before measurement. PPaB-MT content in each film is: (a) 0%; (b) 20%; (c) 30%; (d) 50%. Scale bar: 50 nm. The area of lighter phases decreases with the increase of PPaB-MT content, indicating the lighter phases refer to PVDF-HFP phases. Then the darker phases correspond to PPaB-MT phases.

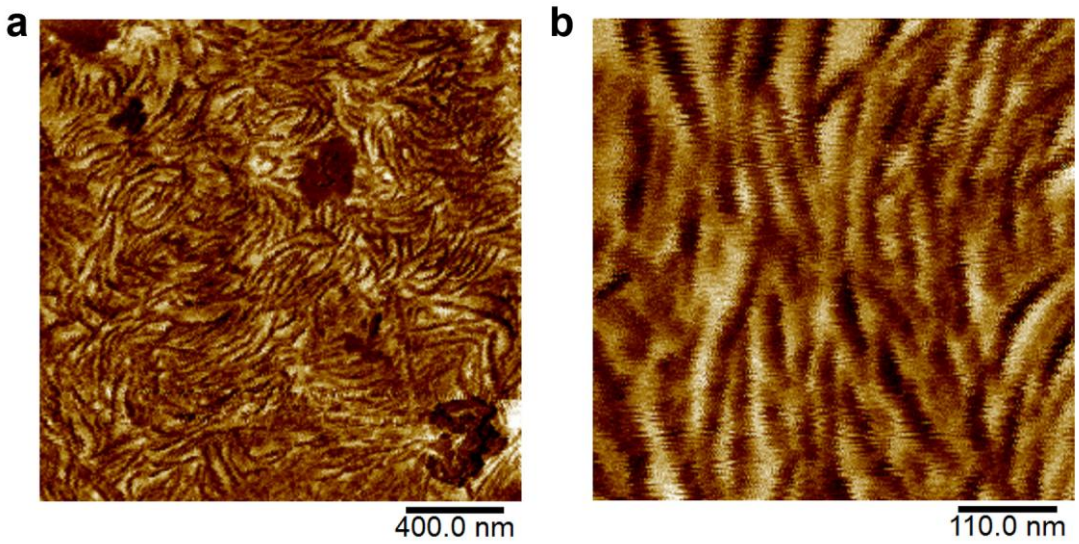

Fig. S16 AFM images of the PPaB-MT/PVDF-HFP/LiTFSI films with PPaB-MT content of 50 wt%. The width of PPaB-MT phases obtained from AFM images is slightly larger than that measured from TEM images, probably due to surface flattening of AFM samples. As AFM can only characterize the surface features of samples while TEM can show the inner structures, we think the width from TEM images is more reliable.

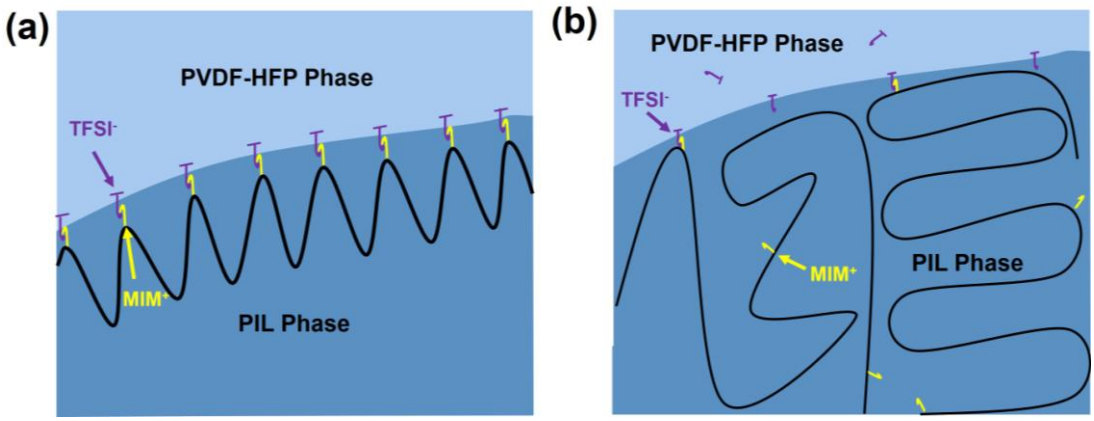

Fig. S17 Schematic illustration of (a) a possible nanophase separation fashion in the PPaB-MT/PVDF-HFP film and (b) a possible microphase separation mode in the PPaB-MT-43/PVDF-HFP film.

Fig. S17a shows a possible fashion for the nanoscale phase separation of the PPaB-MT and PVDF-HFP, in which the TFSI and MIM ions locate at the interface of the two phases and their electrostatic interaction contributes to the nanoscale phase separation. As a comparison, we synthesized a control PIL polymer (PPaB-MT-43) with longer PEG chains (DP=43) and studied its phase separation with PVDF-HFP (Figs. S19-S21). The longer PEG chains decreased the density of MIM/TFSI ion pairs in the blend and thus weakened the electrostatic interaction between the two blended polymers. As a result, microscale rather than nanoscale phase separation took place (Fig. S21), validating the important role of strong electrostatic interactions between two blended polymers in the scale of their phase separation.

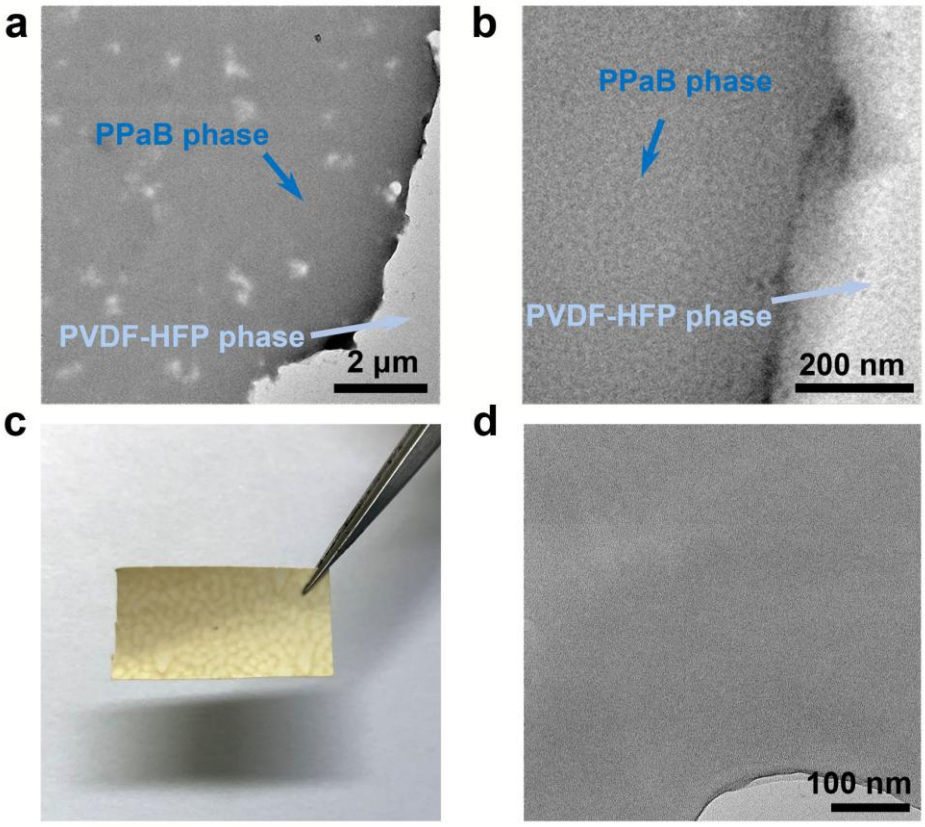

Fig. S18 (a,b) TEM images of the PPaB /PVDF-HFP films with a PPaB content of 50 wt%. (c) Digital photos and (d) TEM image of the SPE films prepared by blending PPaB-MO with PVDF-HFP (PPaB-MO content: 40 wt%). 20 wt% LiTFSI was added into the polymer composites.

PPaB is a neutral polymer with an alternating architecture (Scheme 1 in the main text). When blended with PVDF-HFP, macrocale phase separation took place (Fig. S18a,b). PPaB-MO is the precursor of PPaB-MT (Scheme 1 in the main text). In PPaB-MO, OTs^- ions are present instead of $TFSI^-$. The SPE film prepared by blending PPaB-MO and PVDF-HFP also underwent a macroscale phase separation (Fig. S18c), and nanoscale phase separation could not be observed under TEM (Fig. S18d). These results indicate that both the electrostatic interactions and the presence of TFSI anions are indispensable for the nanophase separation.

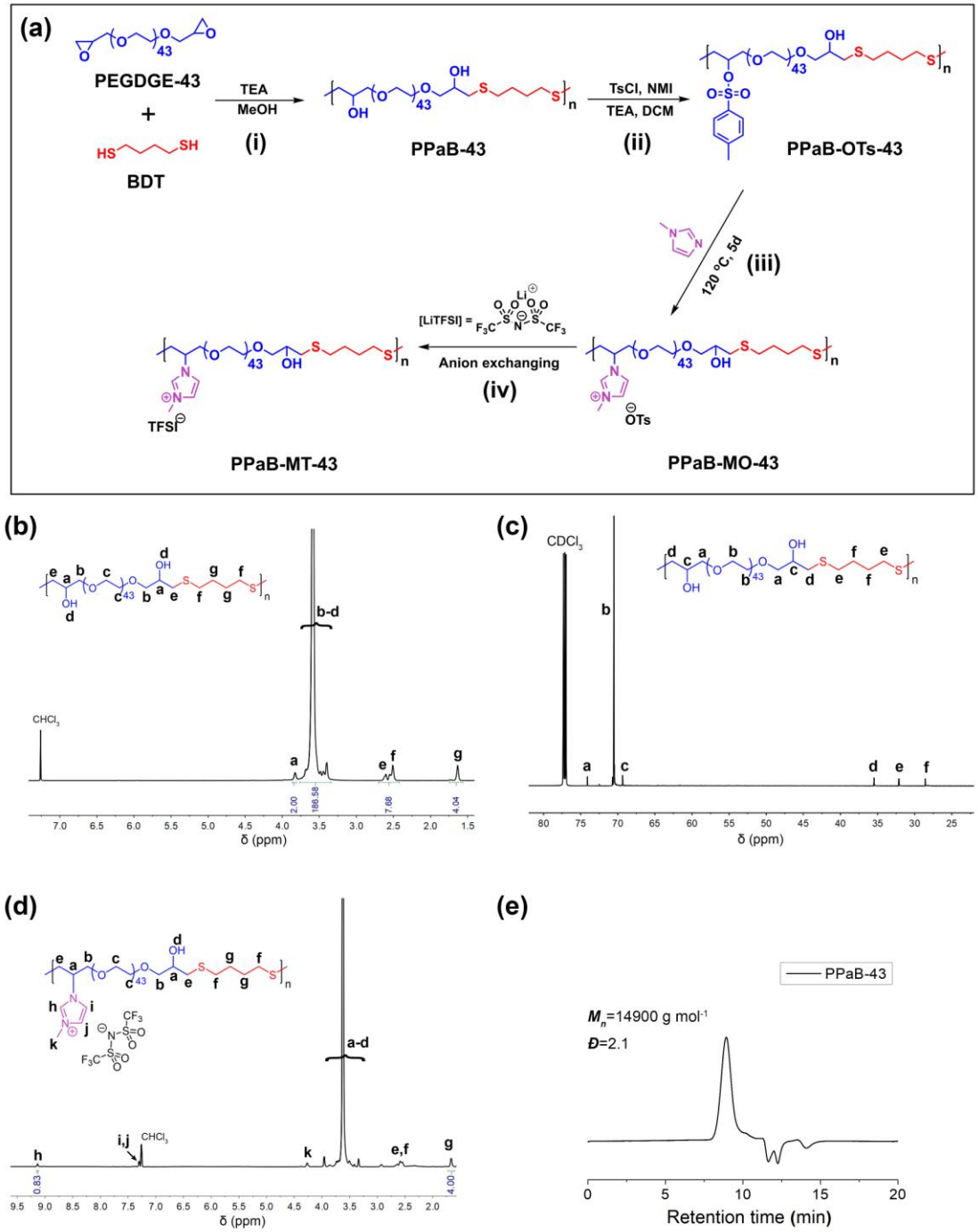

Fig. S19 Synthesis and characterization of a control polymer, PPaB-MT-43 with longer PEG blocks (43 represents the average number of -CH_2CH_2O- units in each PEG segment). (**a**) Synthesis route of PPaB-MT-43. (**b**) ^{1}H NMR and (**c**) ^{13}C NMR of PPaB-43. (**d**) ^{1}H NMR of final product of PPaB-MT-43. (**e**) GPC trace of PPaB-43 measured in DMF against linear polystyrene standard.

The synthesis of PPaB-MT-43 with longer PEG segments was conducted by

replacing the short PEG oligomer (DP=9) in the PEGDG monomer with longer PEG chains (DP=43), as shown in Figure S19a. ^{1}H NMR and ^{13}C NMR spectra of the intermediate and final products show well-assigned peaks (Fig. S19b-d) similar to previous PIL, PPaB-MT (Figs. S1, S2 and S4). According to the integration area of the corresponding peaks in ^{1}H NMR of PPaB-MT-43 (Fig. S19d) and the equation (1), the conversion ratio (ϕ) of the hydroxyl groups to the MIM/TFSI groups is calculated to be 42%, which is comparable with that of PPaB-MT (ϕ=32%). The molar mass of PPaB-43 was measured to be 14,900 g mol^{-1}, and the dispersity (Đ) was 2.1 (Fig. S19e). As a result, the molar mass of PPaB-MT-43 was calculated to be 15,900 g mol^{-1}, which is also comparable with that of PPaB-MT (molar mass: 12,000 g mol^{-1}). It is noted that although with similar molar mass and conversion ratio, the density and the amount of the MIM/TFSI groups in PPaB-MT-43 is lower than those of PPaB-MT due to the presence of the longer PEG blocks.

In summary, the molecular structure of the control polymer, PPaB-MT-43, is analogous to that of PPaB-MT, including alternating architecture, grafting ratio of ionic liquid moieties, and molar mass. Therefore, its phase separation with PVDF-HFP and the ionic conductivity of their SPE can be investigated and compared with those of the SPE formed by PPaB-MT and PVDF-HFP.

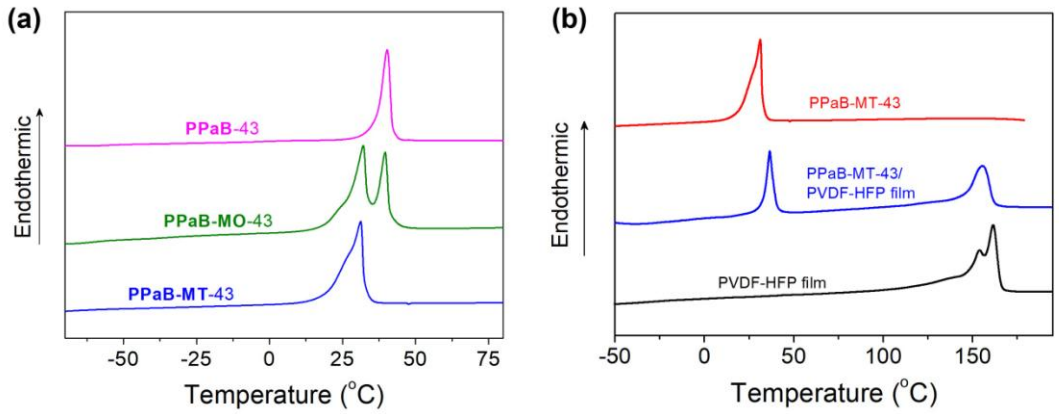

Fig. S20 DSC analysis of PPaB-MT-43 and SPE prepared by blending PPaB-MT-43 and PVDF-HFP. (**a**) DSC traces of the intermediate and final products of PPaB-MT-43. No glass transitions but melting behaviors are observed in these polymers. (**b**) DSC traces of SPE films with a polymer composition of PPaB-MT-43/PVDF-HFP = 4/6 (w/w), and 20 wt% LiTFSI.

Different from PPaB-MT with a T_g = -44.8 ^{o}C, PPaB-MT-43 shows no glass transition temperature but a melting temperature at ~30 ^{o}C (Fig. S20a), indicating the polymer is crystalline due to the longer length of PEG segments. After blending PPaB-MT-43 with PVDF-HFP and LiTFSI, the resulting SPE film shows two endothermic peaks at 35 ^{o}C and 155 ^{o}C (Fig. S20b), which correspond to the melting temperature of PPaB-MT-43 and PVDF-HFP, respectively. The two melting peaks of the SPE film infer that PPaB-MT-43 and PVDF-HFP are immiscible, and their phase separation is expected.

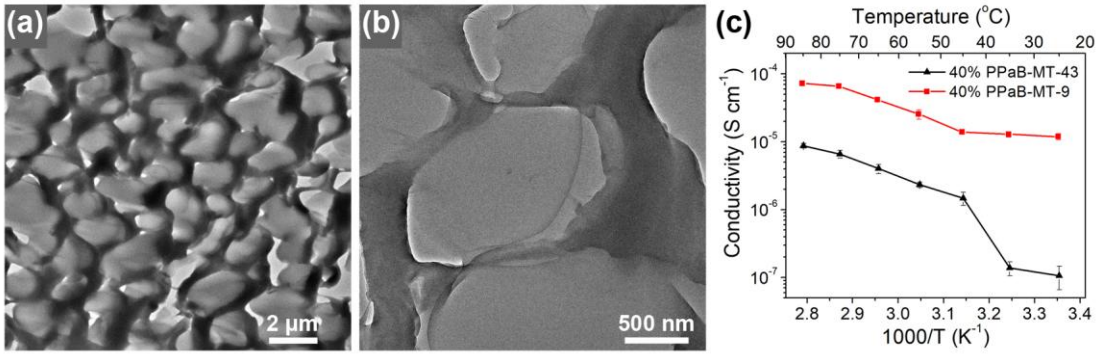

Fig. S21 (a,b) TEM images and (c) ionic conductivity of SPE prepared with PPaB-MT-43 and PVDF-HFP. The composition of the two polymers is PPaB-MT-43/PVDF-HFP = 4/6, and 20 wt% LiTFSI is added. The darker area in TEM images correspond to PIL phase and the lighter phases are PVDF-HFP.

Microscale phase separation occurs in the SPE of PPaB-MT-43/PVDF-HFP. Compared with the PPaB-MT/PVDF-HFP SPE film, the microscale phase separation can be rationalized by the much lower content of ionic liquid moieties on the polymer backbone. The lower density of the ionic pairs weaken the supramolecular interactions between the two blended polymers, leading to the microscale phase separation.

A great increase in ionic conductivity of the SPE of PPaB-MT-43/PVDF-HFP is observed once the temperature exceeds 35 ^{o}C (Fig. S21c), where the PPaB-MT-43 phase start to melt and the mobility of the PEG segments increase.[12] Compared with SPE formed by PPaB-MT, the SPE prepared from PPaB-MT-43 showed two orders of magnitude lower ionic conductivity at 25 ^{o}C and one order of magnitude lower at 85 ^{o}C. Thereby, the phase separation at an increased scale is considered to be an important reason for the obviously reduced ionic conductivity because (a) it enables the aggregation of more and longer PEG blocks, which favors their crystallization, and (b) it cannot form continuous PIL phase throughout the SPE film, which is not beneficial to the ionic conductivity. These results further support our mechanism/interpretation on the contribution of nanophase separation to the high performance of the SPEs prepared from PPaB-MT with short PEG chains.

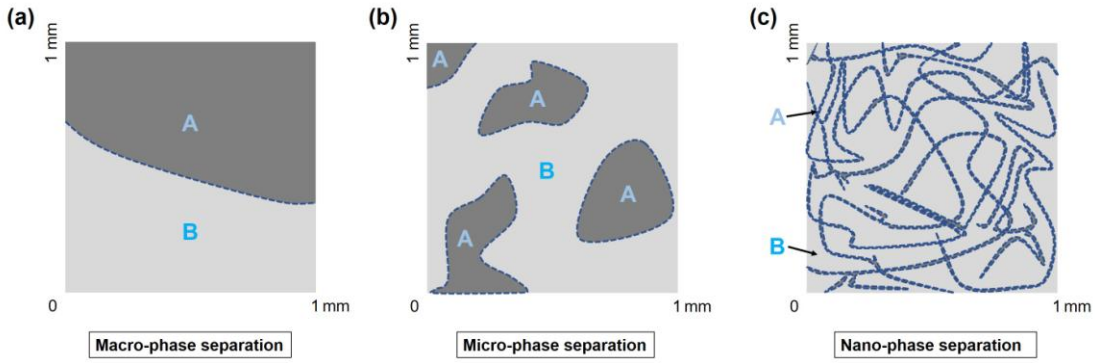

Fig. S22 Schematic illustration of phase separation at different scales. (a) Macro-scale, (b) Micro-scale and (c) Nano-scale phase separation. A and B represent two phases. The blue dashed lines indicate the boundaries between phase A and phase B. Area *A* is the same in all three cases, but the boundary length *l* varies a lot. So it is obvious that APL_b (a) > APL_b (b) > APL_b (c), as $APL_b = A/l$.

To quantitatively evaluate the relationship between the extent of phase separation and ionic conductivity, we conceived a parameter to define the **extent of phase separation** based on TEM images, which is denoted as **area per length of phase boundary** (APL_b) and can be calculated by Eq. (1):

$$APL_b = \frac{A}{l} \qquad (1)$$

where *A* is the total area of the TEM image, and *l* represents the total lengths of all the boundaries between the two phases. By this formula, APL_b is zero if no phase separation happens (*l* is infinity), and APL_b decreases with a decrease in the scale of phase separation: APL_b (macroscales) > APL_b (microscales) > APL_b (nanoscales) (Fig. S22). Based on this equation, we calculated the values of APL_b for different SPEs on the basis of their TEM images and the results are given in Fig. S23. Apparently, the APL_b value decreases from 7.5 to 0.01 as the extent of phase separation increases from macroscale to nanoscale. Furthermore, we established a relationship between ionic conductivity and the extent of phase separation (Fig. S24). It is obviously seen that the ionic conductivity decreases basically with an increase in the APL_b value. This result indicates that the increase of the extent of phase separation (from macroscale to nanoscale) is an effective way to improve the overall ionic conductivity

of the SPEs, which well supports our experimental results.

Description	TEM	Graphic model	APL_b = A/l (μm)	δ (S cm^{-1})
Macroscale phase separation PPaB/PVDF-HFP (50% : 50%)	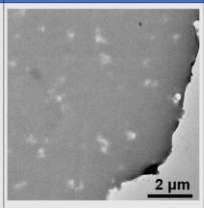	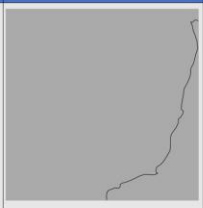	86.8/11.6 = 7.5	1.6×10^{-7} (25 °C) 7.1×10^{-7} (85 °C)
Microscale phase separation PPaB-MT-43/ PVDF-HFP (40% : 60%)	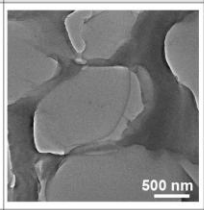		7.0/15.0 = 0.47	1.1×10^{-7} (25 °C) 8.7×10^{-6} (85 °C)
Nanoscale phase separation PPaB-MT/ PVDF-HFP (10% : 90%)	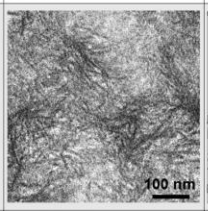	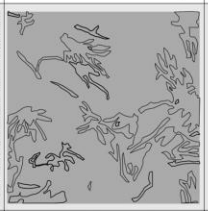	0.51/15.23 = 0.033	6.6×10^{-6} (25 °C) 3.5×10^{-5} (85 °C)
Nanoscale phase separation PPaB-MT/ PVDF-HFP (20% : 80%)	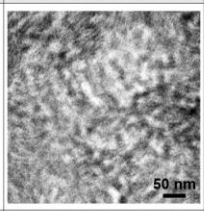	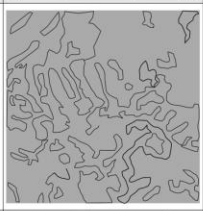	0.23/9.63 = 0.024	9.6×10^{-6} (25 °C) 3.8×10^{-5} (85 °C)
Nanoscale phase separation PPaB-MT/ PVDF-HFP (30% : 70%)	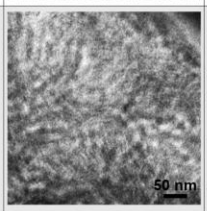	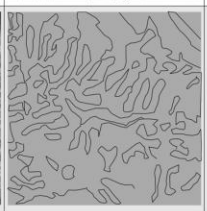	0.20/10.41 = 0.019	1.1×10^{-5} (25 °C) 4.7×10^{-5} (85 °C)
Nanoscale phase separation PPaB-MT/ PVDF-HFP (40% : 60%)	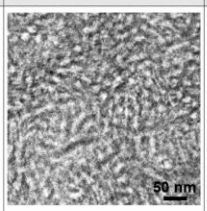	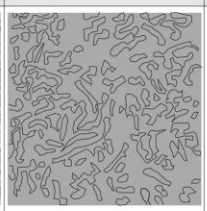	0.20/15.52 = 0.013	1.2×10^{-5} (25 °C) 7.2×10^{-5} (85 °C)
Nanoscale phase separation PPaB-MT/ PVDF-HFP (50% : 50%)	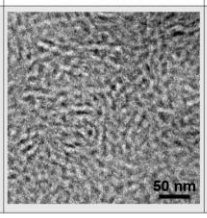	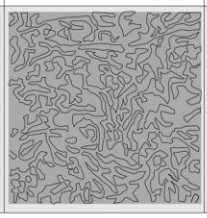	0.12/11.82 = 0.010	1.5×10^{-5} (25 °C) 1.0×10^{-4} (85 °C)

Fig. S23 Calculation of the *extent of phase separation* parameter (APL_b) of different SPEs. The values of APL_b decreased from 7.5 to 0.01 when the phase separation happens at from macrocale to nanoscale.

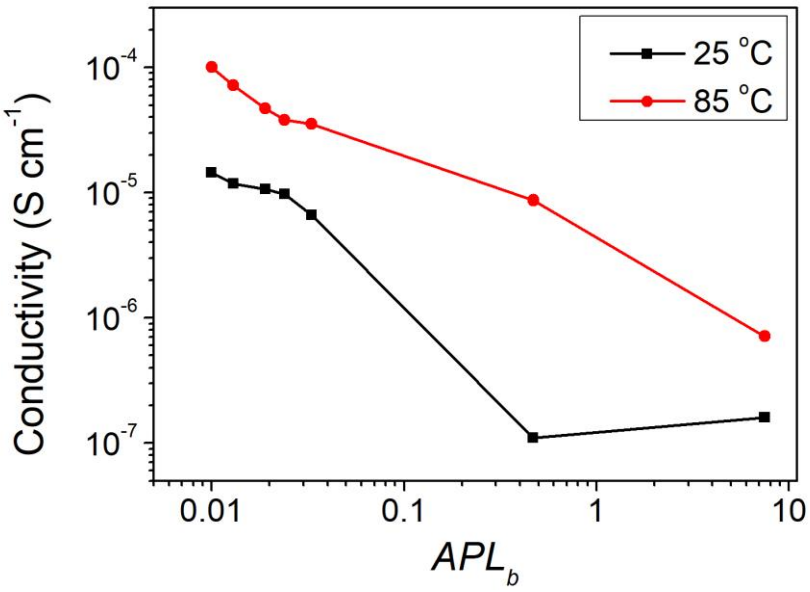

Fig. S24 Ionic conductivity of SPEs against the *extent of phase separation*. Ionic conductivity decreased monotonously with the decrease of APL_b values. The only data point that violates the rule is APL_b = 0.47 at 25 °C, which is caused by the PEG crystallization (see Figs. S20, S21). This conclusion indicates that diminishing phase separation scales may be an effective way to improve the overall conductivity of the SPEs.

3. References

1 F. Schüler, B. Kerscher, F. Beckert, R. Thomann and R. Mülhaupt, *Angew. Chemie - Int. Ed.*, 2013, **52**, 455–458.

2 Y. Fan, D. Zhang, J. Wang, H. Jin, Y. Zhou and D. Yan, *Chem. Commun.*, 2015, **51**, 7234–7237.

3 J. Chen, C. Yu, Z. Shi, S. Yu, Z. Lu, W. Jiang, M. Zhang, W. He, Y. Zhou and D. Yan, *Angew. Chemie - Int. Ed.*, 2015, **54**, 3621–3625.

4 R. Dong, R. Liu, P. R. J. Gaffney, M. Schaepertoens, P. Marchetti, C. M. Williams, R. Chen and A. G. Livingston, *Nat. Chem.*, 2019, **11**, 136–145.

5 H. He, M. Zhong, B. Adzima, D. Luebke, H. Nulwala and K. Matyjaszewski, *J. Am. Chem. Soc.*, 2013, **135**, 4227–4230.

6 H. Awada and C. Daneault, *Appl. Sci.*, 2015, **5**, 840–850.

7 X. Wang, H. Zhu, G. M. A. Girard, R. Yunis, D. R. Macfarlane, D. Mecerreyes, A. J. Bhattacharyya, P. C. Howlett and M. Forsyth, *J. Mater. Chem. A*, 2017, **5**, 23844–23852.

8 N. Mozhzhukhina, A. Y. Tesio, L. P. Mendez De Leo and E. J. Calvo, *J. Electrochem. Soc.*, 2017, **164**, A518–A523.

9 M. Zhang, S. Yu, Y. Mai, S. Zhang and Y. Zhou, *Chem. Commun.*, 2019, **55**, 6715–6718.

10 R. Xu, X. Q. Zhang, X. B. Cheng, H. J. Peng, C. Z. Zhao, C. Yan and J. Q. Huang, *Adv. Funct. Mater.*, 2018, **28**, 1705838.

11 J. Lang, J. Song, L. Qi, Y. Luo, X. Luo and H. Wu, *ACS Appl. Mater. Interfaces*, 2017, **9**, 10360–10365.

12 R. Bouchet, S. Maria, R. Meziane, A. Aboulaich, L. Lienafa, J. P. Bonnet, T. N. T. Phan, D. Bertin, D. Gigmes, D. Devaux, R. Denoyel and M. Armand, *Nat. Mater.*, 2013, **12**, 452–457.